Artefact peaks of pore size distributions caused by unclosed sorption isotherm and tensile strength effect

Wende Lai[1] · Shuo Yang[1] · Yanghui Jiang[1] · Fangyuan Zhao[1] · Zhengjiong Li[1] · Bilal Zaman[1] · Muhammad Fayaz[1] · Xiran Li[1] · Yong Chen[1,2]

Abstract

The pore size distribution (PSD) is an important property of the porous materials, but an accurate and reliable PSD is very difficult to obtain. Quenched Solid Density Functional Theory (QSDFT) is widely used to analyze the pore size distribution. Here, a series of unclosed and closed isotherms of activated carbon were measured and compared. The experimental results revealed the appearance of an artefact peak in the PSD for the unclosed isotherms by employing QSDFT equilibrium model. Moreover, the location of the artificial peak is highly related to the end point of the desorption branch. In addition, tensile strength effect (TSE) illustrates the limit of mechanical stability of liquids in pores, and subsequent cavitation generates an artefact peak at around 2.8 nm. Interestingly, it was found that isotherm data associated with TSE can be used to calculate the total pore volume of all large cavities in which cavitation occurs.

Keywords QSDFT equilibrium model · Tensile strength effect · Pore size distributions · Adsorption · Desorption

1 Introduction

The pore size distribution (PSD) is an important property of the porous materials, which are widely used in energy storage, preparation of supported catalysts, and separation (Chmiola et al. 2006; Meng et al. 2017; Young et al. 2018; Méndez-Morales et al. 2019). Particularly for the porous carbons, which are the main electrode materials for supercapacitance (Xia et al. 2008; Wang et al. 2018), the PSD is closely related to the capacitance performance (Shao et al. 2018), energy density, and volumetric capacitance. For instance, the specific capacitance is improved by a large specific surface area and large pores (Young et al. 2018; Prehal et al. 2017). On the other hand, the large pores are detrimental for the

volumetric capacitance, which is lowered. Relatively recent (2006), it was found that the specific capacitance increases significantly when the size of micropores is less than 1 nm (Wang and Xia 2013; Lu et al. 2018; Zhu et al. 2018). For instance, it was found that a decrease in pore size of activated carbon from 1.3 to 0.65 nm causes the volume specific capacitance to notably increase from 80 to 180 F·cm^{-3} (Prehal et al. 2017). However, despite all methods developed so far, the accurate assessment of the pore size is still challenging (Bergaoui et al. 2018; Jahandar Lashaki et al. 2016; Wongkoblap et al. 2010). Among the methods used to analyze the pore size, nuclear magnetic resonance cryoporometry, mercury intrusion porosimetry, and differential scanning calorimetry thermoporosimetry (Gane et al. 2004), electron microscopy (Young et al. 2018), and gas adsorption (Storck et al. 1998) can be cited. Physical adsorption is the most frequently used method to obtain PSD for microporous and mesoporous materials. The isotherms describing the relationship between the adsorption volume and the relative pressure are measured by using various gases, such as N_2, Ar, CO_2, which are sent on the sample surface in small doses until the entire surface of the sample is covered (Wongkoblap et al. 2010). Then, by applying specific methods and equations to the isotherm, PSDs, surface area, and pore volume are obtained (Smarsly et al. 2005; Gelb and

✉ Yong Chen
ychen2002@163.com

[1] State Key Laboratory of Marine Resource Utilization in South China Sea, Hainan Provincial Key Laboratory of Research On Utilization of Si-Zr-Ti Resources, College of Materials Science and Engineering, Hainan University, 58 Renmin Road, Haikou 570228, China

[2] Key Laboratory of Advanced Energy Materials Chemistry (Ministry of Education), Nankai University, Tianjin 300071, China

Gubbins 1998). For example, the surface area of micropores can be calculated by applying the Langmuir method (Langmuir 1918, 1916) based on a monolayer adsorption. Specific surface area of porous materials can be obtained by Brunauer–Emmett–Teller (BET) theory (Stephen et al. 1938) based on a multilayer adsorption. The capillary condensation normally occurring in a mesoporous material is used to establish a relationship between the relative pressure and the pore diameter, which is described by the Kelvin equation. Barret–Joyner–Halenda (BJH) method based on Kelvin equation can be used to analyze the mesopore size distribution (Barrett et al. 1951). For the analysis a micropore size distribution, Horvath–Kawazoe (HK) method (Horvath and Kawazoe 1983) and Saito–Foley (SF) model (Saito and Foley 1991, 1995) are typically used. HK is generally applied to assess the PSD of activated carbon with slit-shaped pores and SF is applied for the evaluation of PSD of zeolites with cylindrical pores.

In recent years, molecular simulations (Steele 2002; Vuong and Monson 1996; Hirotani et al. 1997) and Non-Local Density Functional Theory (NLDFT) (Tarazona 1985; Tarazona et al. 1987) were developed and used for adsorption characterization of materials, both microporous and mesoporous. NLDFT is a statistical mechanical theory that describes the molecular properties of fluids (Jagiello and Olivier 2013). For this method, a one-dimensional model of pore structure with uniform energy distribution on the surface walls is adopted (Walton and Quirke 1989; Ravikovitch and Neimark 2001, 2002a; Tarazona 1985; Jagiello and Olivier 2013). However, the main shortcoming of the NLDFT model is related to the chemical and geometrical heterogeneity of the pore walls, which are not considered. This is different from the actual situation when the porous materials have rough surface (Ravikovitch et al. 1995, 2000; Olivier 1998). Taking into account the surface roughness, the Quenched Solid Density Functional Theory (QSDFT) (Ravikovitch and Neimark 2006; Landers et al. 2013; Gor et al. 2012) and 2D-NLDFT (Jagiello and Olivier 2013; Puziy et al. 2016; Kwiatkowski et al. 2019) models were developed for the pore structure characterization by gas adsorption.

The different probe gases (N_2, Ar, and CO_2) used to assess the textural properties of a porous material are adsorbed at different temperatures and they exhibit different adsorption behaviours, although their kinetic diameters are similar (0.36, 0.34, and 0.33 nm for N_2, Ar, and CO_2, respectively) (Sing and Williams 2004b). However, the chemical composition of the solid surface is also important, and it is used to select the appropriate gas for the adsorption. Hence, the results of the adsorption measurements for the same sample are different depending on the gas used. Due to its quadrupolar moment, the nitrogen molecule, which is adsorbed at 77 K, interacts with surface functional groups or free ions (Storck et al. 1998). The argon molecule, adsorbed at 87 K, has no quadrupolar moment, it does not exhibit specific interactions with the functional groups, and the adsorption in micropores occurs at a higher relative pressure than for nitrogen, whereas the diffusion rate is higher, the equilibrium is faster reached, and measurement time is shorter. Therefore, smaller pores can be suitably characterized by Ar adsorption with higher precision and accuracy. For CO_2, the adsorption measurements are performed at 273 K. At this temperature, the diffusion is greatly faster, whereas it is insensitive to pores larger than 1.5 nm (Ravikovitch et al. 2000; Jagiello and Thommes 2004) and also has quadrupolar moment.

For porous materials with complex pore structures, such as activated carbon, QSDFT is widely used to analyze PSD. QSDFT is a microscopic model that describes adsorption and more realistically reflects the thermodynamic properties of the fluid in the pore. In the practical applications, a large number of QSDFT theoretical isotherms are developed and they constitute the so-called kernel. The calculation of the theoretical PSDs is based on fitting the theoretical isotherm of the kernel to the experimental data. Hence, the accuracy of pore size calculation is related to the difference between real and theoretical isotherms.

The unclosed isotherms are obtained for some activated carbon or MOFs materials. They obviously deviate from the theoretical isotherm for which the hysteresis loop is closed. However, it is unknown what effect this abnormality may have on the pore size calculation, and most researchers do not realize the difference, they simply using the software to analyze PSD for their porous materials. To properly address this issue, it is important to study the influences of the unclosed isotherm. For this purpose, a series of unclosed and closed isotherms of activated carbon were measured and the corresponding PSDs were calculated by the QSDFT method. In addition, considering the cavitation phenomenon (Ravikovitch and Neimark 2002b; Reber and Bruhwiler 2015), the artefact peak in the PSD curve caused by TSE is explained in detail.

2 Materials and characterization

Five porous carbons were selected for this study and labelled as AC1–AC5. For comparison, graphite with mesopores and macropores in the structure was also analyzed.

The Ar physisorption was used to measure pores size distribution of the solids. Before measurement, each sample was degassed at 300 °C for 5 h. Then, Ar adsorption–desorption measurements were performed on an Autosorb iQ2 (Quantachrome Instruments) at 87 K. The isotherms were recorded and then processed to obtain PSD curve for each solid using QSDFT model within ASiQwin 600 software.

3 Results and discussions

3.1 Unclosed isotherm

For AC1, due to the swelling of non-rigid pores (Lowell et al. 2004) or the near-solid state condensation of the adsorbate at the entrance of pores, the evaporation of fluid from the pore cavity (Maddox et al. 1997) is prevented,

resulting in a very low pressure hysteresis, as shown in Fig. 1a and b. Many similar results have been reported so far (Bailey et al. 1971). Yet, they do not describe the effect of the unclosed isotherm on PSD.

To understand the relationship between the unclosed isotherm and PSDs, four isotherms with different desorption ranges of AC1 were measured (Fig. 1a–d), and QSDFT equilibrium model was employed to calculate the PSD. As shown in Fig. 1a, the adsorption isotherm is a combination
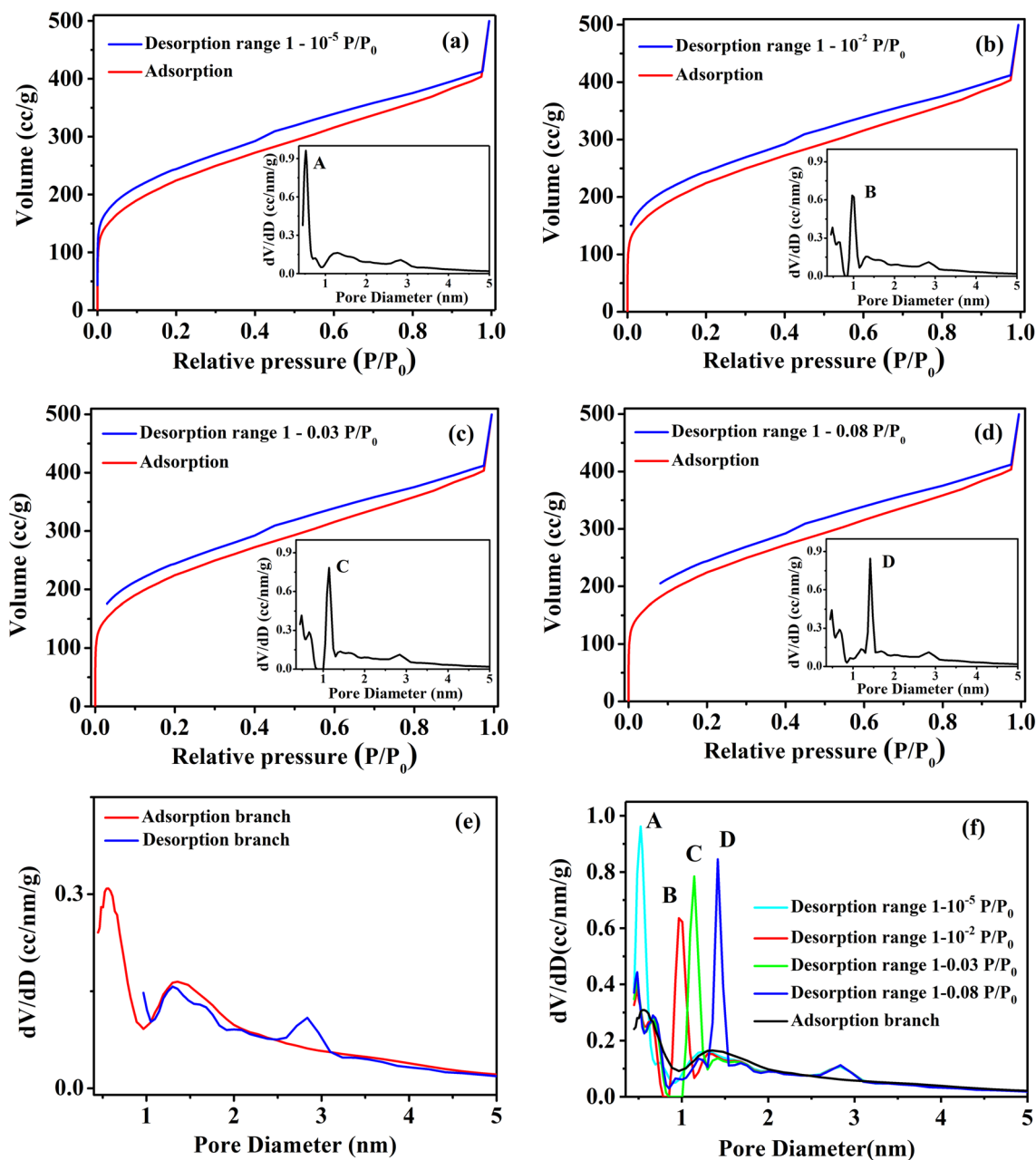

Fig. 1 The isotherms of AC1 with desorption branches measured on ranges of: $1–10^{-5}$ P/P_0 (**a**), $1–10^{-2}$ P/P_0 (**b**), $1–0.03$ P/P_0 (**c**), $1–0.08$ P/P_0 (**d**) and corresponding PSDs (inset) calculated with the equilib-

rium model. PSDs derived from adsorption and desorption branches (**e**) and the comparison of PSDs (**f**)

of type I and type II, indicating the presence of a large number of micropores. However, a very low pressure hysteresis loop is associated with appearance of a peak at 0.5 nm (inset Fig. 1a) when the desorption ends at 10^{-5} P/P_0 (Fig. 1a). However, when the desorption isotherm was recorded in the range $1-10^{-2}$ P/P_0 (Fig. 1b), the corresponding peak in the PSD curve appears at 1 nm while the peak at 0.5 nm almost disappears (inset Fig. 1b). Still, the desorption range for the isotherm displayed in Fig. 1a is larger than that displayed in Fig. 1b, indicating a higher contribution of micropores in the first case. On the other hand, the inset of Fig. 1a does not display a sharp peak at 1 nm. Obviously, this is abnormal, and it is not caused by real pores. When the desorption ranges from 1 to 0.03 and 0.08 P/P_0 (Fig. 1c and d, respectively), the corresponding peaks in PSDs are placed at 1.2 nm (inset Fig. 1c) and 1.4 nm (inset Fig. 1d), respectively. Normally, each peak on the PSD curve corresponds to a step on the desorption branch, which is related to the evaporation of gas from a type pore of a certain size in the micro and mesoporous domains. For example, the peak at 1.5 nm corresponds to a steep desorption step at 0.1 P/P_0 on the isotherm and it would denote the presence of micropores with an average size of 1.5 nm. Comparing the isotherms and PSD curves, the peaks (inset of Fig. 1 b–d) should be related to changes at low relative pressure on the desorption branch. Yet, no such changes can be seen on the desorption branches of the three isotherms. Therefore, it can be affirmed that the peaks at 1, 1.2, and 1.4 nm discussed above do not really correspond to the pores existing in the solid and thus, they are Artefact Peaks (APs). The AP moves with the shift of the end-point on the desorption isotherm. Obviously, the appearance of these APs is related to the non-closure of the isotherm.

To go insight into this phenomenon, the PSD curve for the solid whose isotherm is displayed in Fig. 1b was separately calculated from the adsorption and the desorption branches. The two PSD curves are shown in Fig. 1e. However, when using isotherms to analyze PSD, the analysis range of the equilibrium model is usually set by default to 0–1 P/P_0, e.g., the PSDs in the inset of Fig. 1a–d. However, unlike the PSD obtained by the equilibrium model in Fig. 1b, when using the desorption branch to calculate the PSD in Fig. 1e, the analysis range of the equilibrium model is set as $1-10^{-2}$ P/P_0, which is equal to the actual desorption measurement range. This indicates that there are no other factors affecting the PSD except for the data of desorption branch and the calculation method of the equilibrium model. Figure 1e shows the comparison of the two PSD curves. The PSD curve obtained by the adsorption branch has a more complete micropore distribution. As noticed, the APs visible in the inset of Fig. 1b–d cannot longer be seen on the PSD curves depicted in Fig. 1e. Therefore, it is confirmed that the peaks (B, C, D) are erroneous. Moreover, there is no

AP which is produced by the tensile strength effect (TSE) at 2.8 nm. Nevertheless, the PSDs of the two are similar.

Figure 1f shows the comparison of the adsorption-based PSD and desorption-based PSDs (inset of Fig. 1a–d) of AC1. Indeed, the adsorption-based PSD curve shows no sharp distribution peak (such as peaks A, B, C, and D). Moreover, there was no AP at ~ 2.8 nm. However, except for these differences, adsorption-based PSD and desorption-based PSD exhibit a similar PSD, indicating that the adsorption branch shows more reliable PSD information. In fact, except for peak A, the PSD curves that are below 1 nm of adsorption-based PSD are somewhat different from other PSDs because the DFT method is essentially a fitted theoretical isotherm to the experimental data. Therefore, although it uses the same low-pressure data, the different fits of the method to the different upper P/P_0 ranges may slightly alter the fit in the low-pressure range. However, the PSD message (and how interpret these PSDs) is the same: a distribution of pores from 0.4 to 1 nm.

As shown in Fig. 2a, AC2 activated carbon mainly contains micropores while the desorption and adsorption branches overlap in the low-relative pressure range. Although the relative pressure ranges of the desorption branch are different, i.e., $1-10^{-2}$ (Fig. 2a), 1–0.03 (Fig. 2b) and 1–0.08 P/P_0 (Fig. 2c), the corresponding PSD curves (Fig. 2d) calculated with the equilibrium model are similar. Therefore, if the desorption and adsorption branches overlap below 0.4 P/P_0, APs similar to those in the inset of Fig. 1b–d do not appear in the PSD curves, confirming that such peaks are associated with the non-closure of isotherm. In the PSD curves shown in Fig. 2d, the adsorption-based PSD does not have the AP which is produced by the TSE; except for this difference, it rather has the same PSD as others. This shows that an adsorption isotherm can provide more reliable PSD information because there is less negative information affecting the PSD.

As shown in Fig. 3a, the isotherm displays two steep desorption steps caused by TSE at 0.4 P/P_0 and non-closure, respectively. The non-closure causes an AP at 1 nm, and the TSE causes an AP at 2.8 nm (inset Fig. 3a). It is obvious that the origins of these APs are different.

The desorption isotherm of AC3 is measured from 1 to 0.3 P/P_0 (Fig. 3b). Note that these desorption data can only be used to calculate the pore size larger than 2.3 nm. Indeed, the inset of Fig. 3b (red curve) shows no pore size distribution below 2.3 nm. On the other side, the grey curve illustrated in the inset of Fig. 3b displays pores with size smaller than 2.3 nm. However, these data cannot be provided by the desorption branch, so they can only be associated with the adsorption branch, since the data below 0.03 P/P_0 are not available. In this case, the equilibrium model takes the data in the range of 0–0.3 P/P_0 as if they were from the adsorption isotherm. This situation is valid when the two branches of
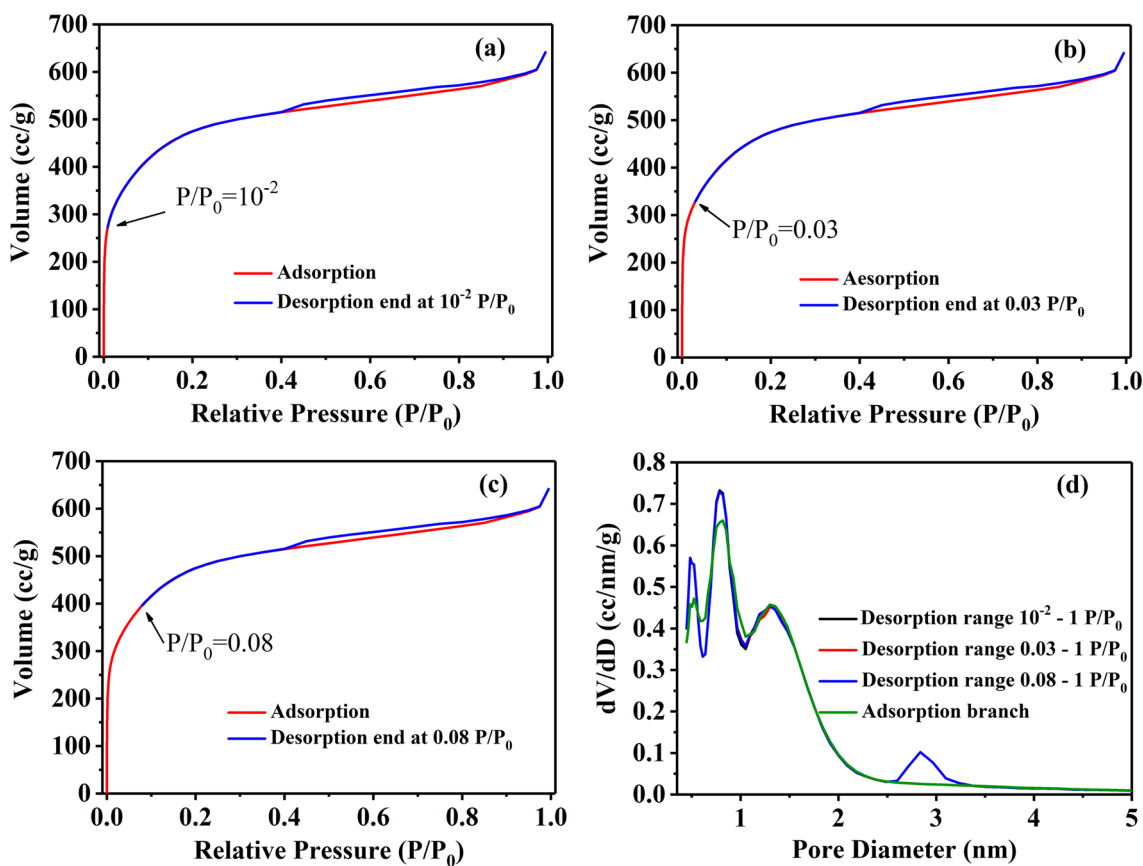
Fig. 2 The desorption isotherms of AC2 end at 10^{-2} (**a**), 0.03 (**b**), and 0.08 P/P$_0$ (**c**), and the corresponding PSDs (**d**)
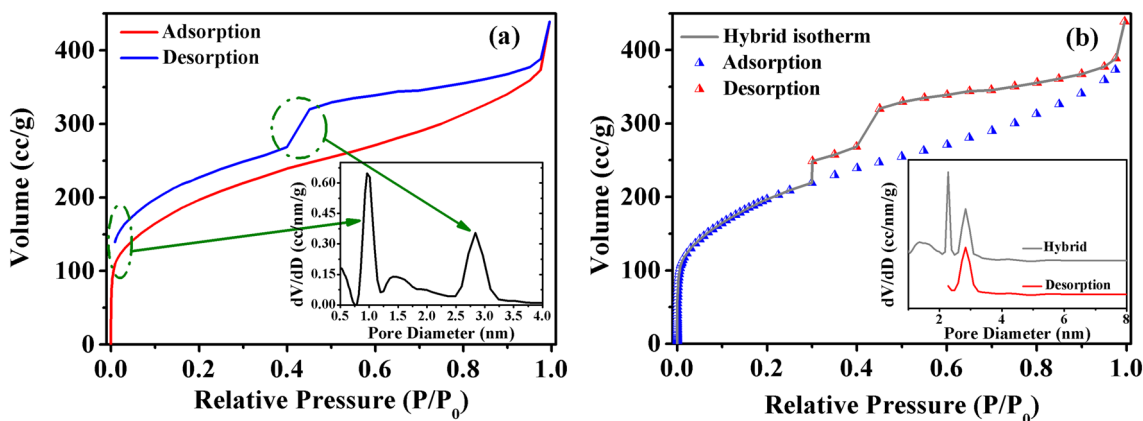

Fig. 3 The isotherm of AC3 (**a**) and corresponding PSDs (inset) calculated with the equilibrium model, and the desorption isotherm measured in the range of 1–0.3 P/P$_0$ (**b**) and corresponding PSDs (inset)

the isotherm close at 0.4 P/P$_0$ (Ar, 87 K) and then overlap at lower relative pressures. Hence, at relative pressure below 0.4, the DFT model analyzes a hybrid isotherm consisting of adsorption and desorption branches, as shown in Fig. 3b. The isotherm is forced closed generating a steep desorption step, which is translated as an AP at 2.3 nm in the PSD curve

(inset Fig. 3b). Therefore, a non-closed isotherm causes an AP and thus, an erroneous assessment of the pore size.

These findings show that the measurement of full desorption range from 1 to 10^{-7} P/P$_0$ or limiting the relative pressure range (equal to the real desorption measurement range) of the QSDFT calculations may prevent AP caused

by non-closure from appearing. However, measuring the full desorption range takes too long time while the delayed evaporation produces a steep decrease, resulting in the appearance of APs at 0.5 nm in the PSD curve, as shown in the inset of Fig. 1a. On the other side, narrowing the relative pressure range for the QSDFT calculations does not consider a part of micropores. By contrary, these problems can be elegantly solved using the adsorption isotherms to calculate PSDs.

It is known that a few of carbon materials have completely reversible isotherms. Figure 4a shows the Ar isotherm of AC4 recorded at 87 K for which the adsorption and desorption branches almost overlap. The isotherms were analyzed by applying adsorption model and equilibrium model, respectively. The corresponding PSD curves are almost the same. Therefore, in such cases, it is feasible to select the equilibrium model to calculate the pore size distribution.

In addition, 0.4 P/P_0 is considered the limit of hysteresis according to TSE. Below 0.4 P/P_0, adsorption and desorption are reversible (Coasne 2016) except for some special materials, such as some activated carbon and MOFs. To accurately evaluate the pore size distribution irrespective of the desorption mechanisms, various mathematical models should be developed. If the desorption end-point of the unclosed isotherm is above 0.4 P/P_0, the obtained results from fitting the models may differ from those obtained below 0.4 P/P_0. Figure 5a depicts the physisorption isotherms (Ar, 87 K) of AC3 whose desorption measurement range are at 1–0.4, 1–0.5, and 1–0.6 P/P_0. Unlike the isotherm unclosed below 0.4 P/P_0, the gradual broad AP at 2.8 nm can be observed (Fig. 5b). However, left end-points are the same for APs of all three PSD curves, meaning that the adsorption and desorption branches were considered closed at 0.4 P/P_0 when the DFT model was applied. To verify this hypothesis, two isotherms (Ar, 87 K) of the same graphite sample, mainly containing mesopores and macropores, were measured. For one of the isotherms, the desorption branch was measured

in the range of 1–0.52 P/P_0 and for the other one, the isotherm closes at 0.4 P/P_0 (Fig. 5c). Despite this difference, the obtained PSD curves are similar (Fig. 5d), consistent with the assumption discussed above regarding the closure of the isotherm at 0.4 P/P_0.

3.2 Tensile strength effect

TSE is an important factor affecting the PSDs calculated by QSDFT. When the tension of the condensed liquid in pores reaches the tensile strength, the liquid evaporates from pores and a forced closure of the hysteresis loop at 0.42–0.5 P/P_0 for N_2 (77 K) (Reber and Bruhwiler 2015) or 0.35–0.45 P/P_0 for Ar (87 K), such as step AB in Fig. 6a. The closure step caused by TSE is a frequent phenomenon occurring for the materials giving isotherms with types H3 and H4 hysteresis loops (Thommes 2010; Lowell et al. 2004). In this case, if desorption isotherm is used to analyze PSD, it causes an AP around 2.8 nm (Fig. 6b). But this AP cannot be observed on the PSD derived from the adsorption branch, implying that the pore distribution peak at 2.8 nm does not actually exist. The relationship between TSE and AP is explained below in the text.

In mesopores, the capillary condensation of the adsorbed gas occurs, forming a meniscus-shaped liquid–vapor interface. Before reaching the condensed state, the adsorbed multilayer is metastable. Overcoming the nucleation energy barrier of liquid phase nucleation requires higher pressure than the capillary evaporation (Saam and Cole 1975; Thommes 2010). During desorption process, the condensed phase evaporates via meniscus-shaped liquid–vapor interface at equilibrium condition, called near-equilibrium evaporation. As shown in Fig. 6a, the BC step is associated with the near-equilibrium evaporation. Thus, the pressure needed for evaporation is lower than that for condensation (Lowell et al. 2004). As a result, a hysteresis loop appears on the adsorption–desorption isotherm.
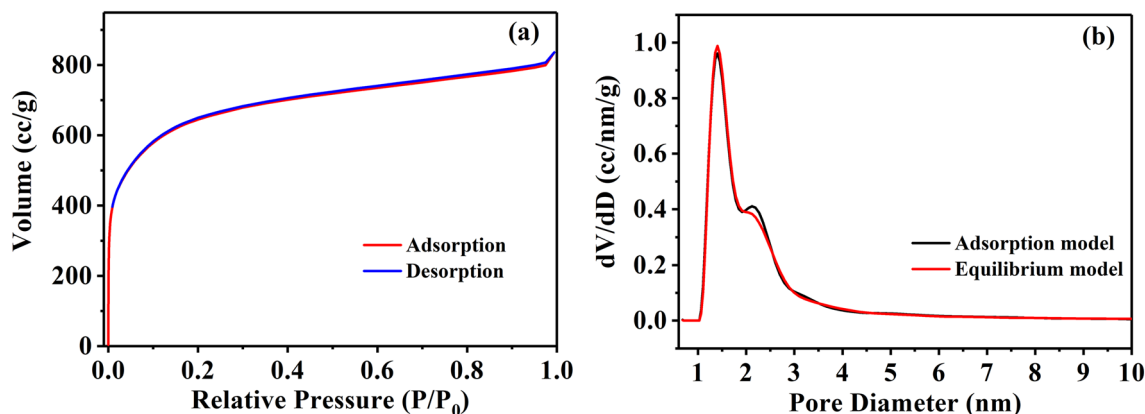

Fig. 4 Ar adsorption–desorption isotherm (**a**) of AC4 and the PSD curves (**b**) obtained by applying adsorption and equilibrium models
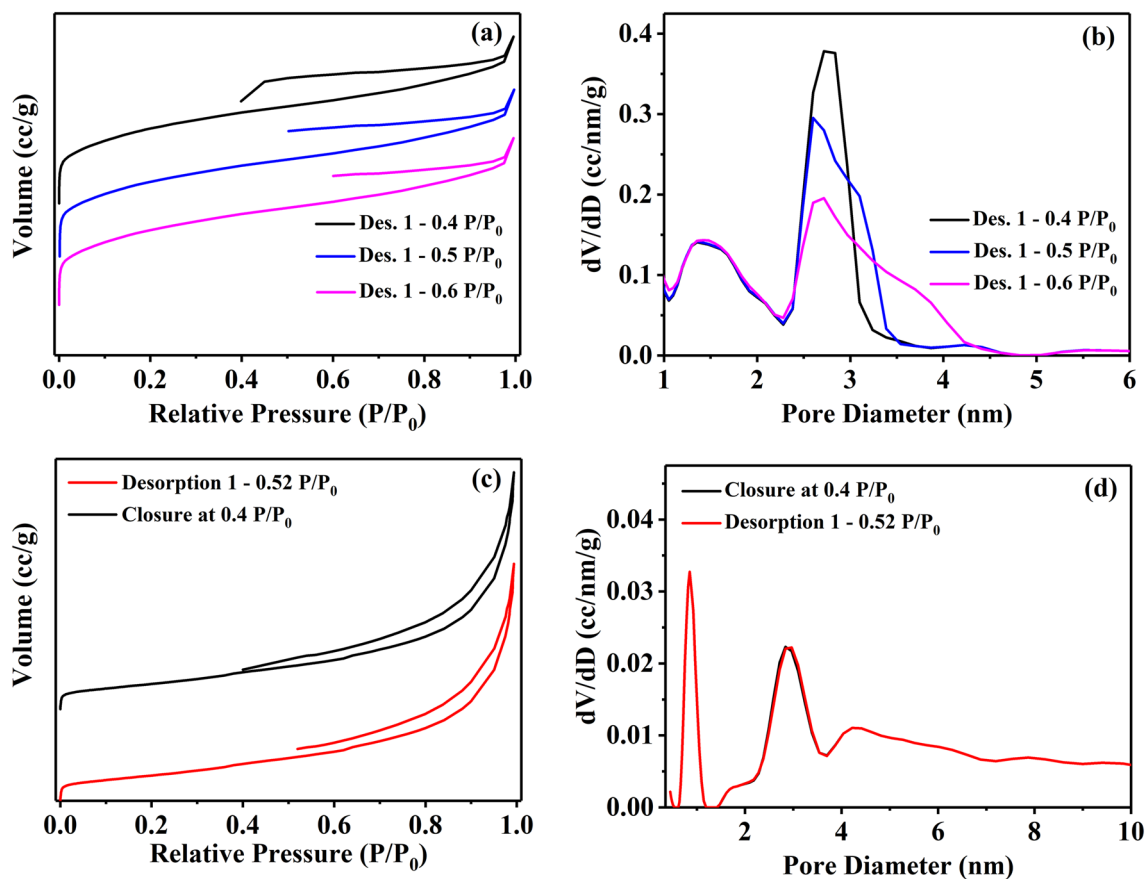
Fig. 5 Ar physisorption (87 K) unclosed isotherms with different desorption ranges and corresponding PSDs of AC3 (**a**, **b**). Ar physisorption isotherms and PSDs of graphite sample (**c**, **d**)
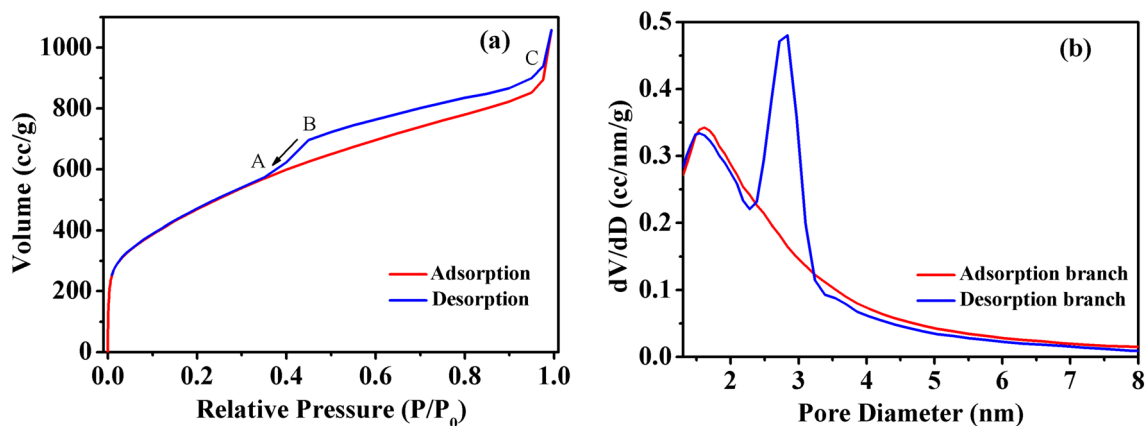

Fig. 6 Isotherm of AC5 (**a**) and corresponding PSDs (**b**) derived from adsorption and desorption branches

Considering that the contact angle between the liquid and the pore wall is zero, the relationship between the pore radius r (cylindrical geometry) and the evaporation pressure can be described by Kelvin equation (Eq. 1):

$$ln\frac{P}{P_0} = -\frac{2\gamma V_m}{r_m RT} \tag{1}$$

$$r = r_m + t \tag{2}$$

where P is the vapour pressure of meniscus surface and P_0 is the vapour pressure of a plane surface, γ is the surface tension coefficient, V_m is the molar volume of liquid, R is the universal gas constant, and T is the absolute temperature (K). t is the thickness of the adsorbed multilayer and r_m is the radius of curvature of the liquid phase at equilibrium. r_m decreases as the relative pressure, P/P$_0$, decreases. If the radius of curvature of the liquid phase is higher than r_m, evaporation occurs. Based on this equation, BJH model was developed to calculate PSD, but it failed when applied to micropores (Groen et al. 2003).

There is a critical relative pressure $(P/P_0)_{TSE}$ (corresponding to the diameter $d_{TSE} = 2r_{TSE} = 2 r_m + 2t$), which defines the capillary condensation limit (Coasne 2016; Kadlec and Dubinin 1969). Above this critical relative pressure, the liquid phase tension (τ) in the pores increases as the relative pressure decreases. The relationship between liquid phase tension, relative pressure, and r_m can be described by the following equations (Gregg and Sing 1982):

$$\tau = -\frac{RT}{V_m}\ln\frac{P}{P_0} \tag{3}$$

$$\tau = \frac{2\gamma}{r_m} \tag{4}$$

When P/P$_0$ reaches the critical value $(P/P_0)_{TSE}$, the liquid phase tension, τ, reaches the tensile strength τ_0 (Kadlec and Dubinin 1969; Gregg and Sing 1982; Burgess and Everett 1970). Then, the capillary condensation liquid phase becomes unstable and evaporates (Sing and Williams 2004a; Gregg and Sing 1982; Sing et al. 2014) and the diameter of pores occurring evaporation at $(P/P_0)_{TSE}$ is d_{TSE}. The τ_0 is a constant for a given adsorbate at a given temperature (Ravikovitch and Neimark 2002b) and has been discussed by Burgess and Everett (1970), Kadlec and Dubinin (1969). For N$_2$ adsorption–desorption measurement (77 K), the theory diameter (d_{TSE}) of pores which occur TSE is 3.44 nm, according to calculations of Sonwane and Bhatia (1998). This value is close to the experimental value (3.6 nm) (Gregg and Sing 1982; Coasne 2016). For Ar adsorption–desorption measurement (87 K), the diameter d_{TSE} approximately is about 4 nm (Coasne 2016; Nguyen et al. 2013b; Reber and Bruhwiler 2015) for cylindrical geometry and 3 nm for slit geometry.

TSE only indicates the limit of capillary condensation when the material has only pores with cylindrical geometry. In this case, if the pore diameter is larger than the diameter (d_{TSE}), near-equilibrium evaporation will occur. If pore diameter is smaller than the d_{TSE}, adsorption and desorption are reversible (Coasne 2016). Throughout the desorption process, the evaporation pressure is related to the pore size and geometry (Coasne 2016). It is worth underlining that only the pores with cylindrical geometry pores do not cause an AP.

In reality, the porous structure of materials is complex. Pores of different size are interconnected and they are come in contact with the gas phase by narrow channels (Fig. 7a). During the adsorption process, the pressure of pore filling is associated with pore size. Fluid first fills the narrow channels and then fills the larger pore cavities, which makes the adsorption isotherm more reliable to obtain information about the pore size. During the desorption process, the fluid in large pore cavities evaporates via the narrow channels. If the diameter of these channels is higher than the diameter (d_{TSE}), the pressure needed for evaporation highly depends on the diameter of narrow channels. After the evaporation

Fig. 7 Schematic diagram of a complex pore network structure (**a**) and cavitation: pore filled with liquid (**b**), formation of bubbles in pore and liquid phase evaporation from channel (**c**), narrow channel filled with fluid while the pore cavity is emptied (**d**), liquid evaporation from the narrow channel (**e**)
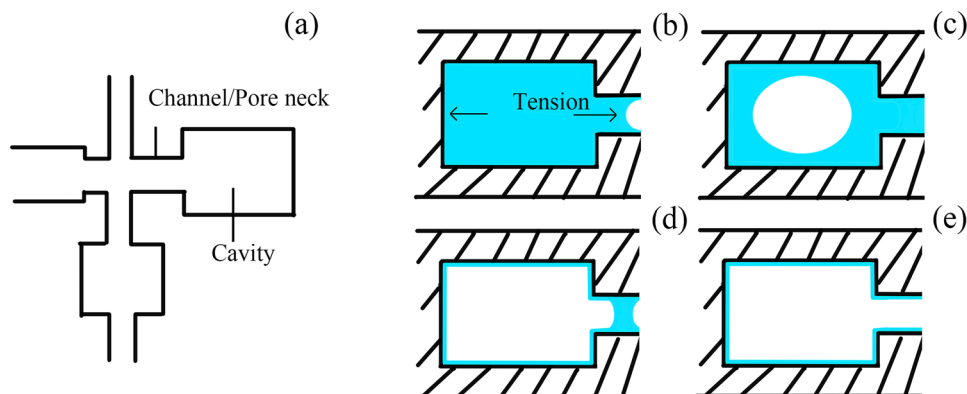
of fluid from the narrow channels, the fluid in the larger pore cavities evaporates suddenly. This phenomenon is referred to as pore blocking (Ravikovitch and Neimark 2002b). In this case, the desorption isotherm contains information on the size of narrow channels, but cannot give accurate pore size information on the larger pore cavities. However, if the diameter of narrow channels is smaller than the d_{TSE}, the cavitation occurs (Ravikovitch and Neimark 2002b; Reichenbach et al. 2011; Nguyen et al. 2013b). Cavitation extends the hysteresis to the critical pressure $(P/P_0)_{TSE}$ and the fluid in larger pore cavities evaporates suddenly due to TSE and causes a steep decrease on the desorption isotherm. In this case, the evaporation does not occur at the theoretical evaporation pressure determined by the pore size, but at the critical pressure determined by TSE. Therefore, the desorption isotherm not contains information on the size of narrow channels and larger pore cavities. Moreover, as discussed above, the pore shape and structure change the shape of the hysteresis loop.

Based on the cavitation phenomenon (Sarkisov and Monson 2001; Ravikovitch and Neimark 2002b), the hysteresis end-point at 0.4 P/P_0 is described in detail. In a complex pore structure, larger pore cavities are connected to the bulk gas phase via narrow channels. If the diameter of narrow channels is smaller than the diameter (d_{TSE}), the liquid phase tension in pore cavities increases with decreasing pressure (Fig. 7b) until reaches the tensile strength at the critical pressure $(P/P_0)_{TSE}$. At this moment, the liquid phase reaches the thermodynamic stability limit. As the pressure continues to decrease, the distance between the molecules in the liquid increases and bubbles nucleation occurs in the large pore cavities (Fig. 7c). As a result, the volume of gas–liquid mixed phase is expanded and the original meniscus of narrow channels disappears. The molecules of the liquid phase evaporate from the narrow channels and diffuse into the bulk gas phase while they are replaced by new molecules coming from the pore cavity (Sarkisov and Monson 2001). Due to the small enough diameter, the narrow channels are permanently filled with fluid (Fig. 7d) as the pore cavity empties. Finally, the liquid phase from these channels evaporates (Fig. 7e) at pressure related to the pore size of channels.

The occurrence of cavitation needs to satisfy several conditions, as follows, (1) the porous materials have large pore cavities connected to the bulk gas phase via narrow channels, (2) the diameter of the narrow channels is smaller than the diameter (d_{TSE}) (Ravikovitch and Neimark 2002b; Rasmussen et al. 2010; Coasne 2016; Thommes et al. 2006), and (3) the relative pressure reaches critical pressure when desorption occurs. The critical pressure $(P/P_0)_{TSE}$ depends on adsorbate, adsorption temperature, and pore geometry (Ravikovitch and Neimark 2002b).

Because of the AP, TSE is misleading for the pore size analysis. However, seen from another perspective, the

isotherm data associated with TSE can be used to calculate the total pore volume of all large cavity in which cavitation occurs.

To demonstrate this theory, the AC5 activated carbon is taken an example. In the range of 0.35 to 0.45 P/P_0 (Fig. 6a), the evaporating adsorbate comes from cavitation and equilibrium evaporation (Cychosz et al. 2017; Cychosz and Thommes 2018). That means that the volume of desorbed molecule coming from cavitation is the difference of the total desorbed volume and the desorbed volume coming from equilibrium evaporation. Between 0.35 and 0.45 P/P_0, the total desorbed volume is obtained from the desorption branch, whereas the desorbed volume coming from the equilibrium evaporation is obtained from the adsorption branch. The cavitation pore volume can then be calculated by converting these desorbed volumes into pore volumes.

Here, the cavitation pore volume is calculated by using the cumulative pore volume. In the range of 0.35–0.45 P/P_0, the cumulative pore volume obtained from the desorption branch is the sum of the volume of large cavities in which cavitation occurs and the volume of pores in which equilibrium evaporation occurs. The cumulative pore volume obtained from the adsorption branch is the volume of pores in which equilibrium evaporation should occur between 0.35 and 0.45 P/P_0. Therefore, the total pore volume of large cavities in which cavitation occurred can be calculated by the cumulative pore volumes obtained from the adsorption and desorption branches.

From Fig. 6a, the steep desorption step between 0.35 and 0.45 P/P_0 causes an AP in range of 2.38–3.24 nm (Fig. 6b). Hence, between 0.35 and 0.45 P/P_0, the volume of the desorbed molecules is converted to the cumulative pore volume in the range of 2.38–3.24 nm. In a similar way, on the adsorption branch, between 0.35 and 0.45 P/P_0, the volume of adsorbate is converted to the cumulative pore volume in the range 2.38–3.24 nm. The total volume of cavities in which cavitation occurred is equal to the difference of cumulative pore volumes obtained from the desorption and adsorption branches. The cumulative pore volumes are shown in Table 1. It can be deduced from Table 1 that the total volume of cavities associated with the cavitation is 0.135 cm^3/g. Therefore, TSE can contribute to the analysis

Table 1 Cumulative pore volume of AC5 calculated from QSDFT

Pore size range (nm)	Cumulative pore volume obtained on the desorption branch (cm^3/g)	Cumulative pore volume obtained on the adsorption branch (cm^3/g)
0–2.38	0.606	0.635
0–3.24	0.881	0.775
2.38–3.24	0.275	0.140

of pore structure and to estimate the total volume of large cavities related to the occurrence of cavitation.

The idea that analyzes the pore structure using the desorption branch and TSE is compared with other theories. Most theories of pore structure analysis focus on the calculation of PSD. If only PSD is required, the adsorption branch can provide more reliable PSD information. But for samples having the same PSD, the adsorption isotherm hardly distinguishes the differences in pore structure because their adsorption isotherms are similar (Nguyen et al. 2013a). However, multiple physical phenomena during the desorption process show some information of pore structure, such as pore blocking and cavitation associated with TSE, which will be reflected in the desorption isotherm. Both phenomena can be used to confirm the existence of inkbottle-like pore structure. Some researchers connect many physical phenomena in the desorption process with the pore structure and determine the possible pore structure by the geometry of the hysteresis loop (Nguyen et al. 2013a; Cychosz et al. 2017). And, the desorption branch and TSE can be used to calculate the total volume of larger pore cavities in which cavitation occurs. Thus, in addition to determining the pore structure, the overall message of the pore structure in the sample can be evaluated to some extent.

4 Conclusions

An artefact peak appears on the pore size distribution if QSDFT equilibrium model is used to analyze an unclosed adsorption–desorption isotherm. TSE is also prone to generate an artefact peak around 2.8 nm. Hence, to accurately reflect the pore size distribution, the pores should be characterized by calculating the PSD on the adsorption branch. However, the isotherm data associated with TSE can be used to calculate the total pore volume of all large cavities in which cavitation occurs based on the difference between the cumulative pore volumes obtained by desorption branch and adsorption branches in the range of 0.35–0.45 P/P_0 (Ar, 87 K). This idea can help researchers to better understand the pore structure of the porous material. These mean that both adsorption and desorption branches of the isotherm can be used to evaluate the porosity. Hence, the adsorption branch is useful to evaluate the pore size distribution, whereas the desorption branch is useful to analyze the pore structure.

References

Bailey, A., Cadenhead, D.A., Davies, D.H., Everett, D.H., Miles, A.J.: Low pressure hysteresis in the adsorption of organic vapours by porous carbons. T. Faraday Soc. **67**, 231–243 (1971)

Barrett, E.P., Joyner, L.G., Halenda, P.P.: The determination of pore volume and area distributions in porous substances. I. Computations from nitrogen isotherms. J. Am. Chem. Soc. **73**(1), 373–380 (1951)

Bergaoui, M., Aguir, C., Khalfaoui, M., Villarroel-Rocha, J., Reinert, L., Enciso, E., Duclaux, L., Barrera, D., Sapag, K.: On the computer simulations of carbon nanoparticles porosity: statistical mechanics model for CO_2 and N_2 adsorption isotherms. Adsorption **24**(8), 769–779 (2018)

Burgess, C.G.V., Everett, D.H.: The lower closure point in adsorption hysteresis of the capillary condensation type. J. Colloid Interface Sci. **33**(4), 611–614 (1970)

Chmiola, J., Yushin, G., Gogotsi, Y., Portet, C., Simon, P., Taberna, P.L.: Anomalous increase in carbon capacitance at pore sizes less than 1 nanometer. Science **313**(5794), 1760–1763 (2006)

Coasne, B.: Multiscale adsorption and transport in hierarchical porous materials. New J. Chem. **40**(5), 4078–4094 (2016)

Cychosz, K.A., Guillet-Nicolas, R., Garcia-Martinez, J., Thommes, M.: Recent advances in the textural characterization of hierarchically structured nanoporous materials. Chem. Soc. Rev. **46**(2), 389–414 (2017)

Cychosz, K.A., Thommes, M.: Progress in the physisorption characterization of nanoporous gas storage materials. Engineering **4**(4), 559–566 (2018)

Gane, P.A.C., Ridgway, C.J., Lehtinen, E., Valiullin, R., Furó, I., Schoelkopf, J., Paulapuro, H., Daicic, J.: Comparison of NMR cryoporometry, mercury intrusion porosimetry, and DSC thermoporosimetry in characterizing pore size distributions of compressed finely ground calcium carbonate structures. Ind. Eng. Chem. Res. **43**(24), 7920–7927 (2004)

Gelb, L.D., Gubbins, K.E.: Characterization of porous glasses: simulation models, adsorption isotherms, and the Brunauer–Emmett–Teller analysis method. Langmuir **14**(8), 2097–2111 (1998)

Gor, G.Y., Thommes, M., Cychosz, K.A., Neimark, A.V.: Quenched solid density functional theory method for characterization of mesoporous carbons by nitrogen adsorption. Carbon **50**(4), 1583–1590 (2012)

Gregg, S.J., Sing, K.S.W.: Adsorption, surface area and porosity. Academic Press, London (1982)

Groen, J.C., Peffer, L.A.A., Pérez-Ramírez, J.: Pore size determination in modified micro- and mesoporous materials. Pitfalls and limitations in gas adsorption data analysis. Microporous Mesoporous Mater. **60**(1–3), 1–17 (2003)

Hirotani, A., Mizukami, K., Miura, R., Takaba, H., Miya, T., Fahmi, A., Stirling, A., Kubo, M., Miyamoto, A.: Grand canonical Monte Carlo simulation of the adsorption of CO_2 on silicalite and NaZSM-5. Appl. Surf. Sci. **120**(1), 81–84 (1997)

Horvath, G., Kawazoe, K.: Method for the calculation of effective pore size distribution in molecular sieve carbon. J. Chem. Eng. Jpn. **16**(6), 470–475 (1983)

Jagiello, J., Olivier, J.P.: 2D-NLDFT adsorption models for carbon slit-shaped pores with surface energetical heterogeneity and geometrical corrugation. Carbon **55**, 70–80 (2013)

Jagiello, J., Thommes, M.: Comparison of DFT characterization methods based on N_2, Ar, CO_2, and H_2 adsorption applied to carbons with various pore size distributions. Carbon **42**(7), 1227–1232 (2004)

Jahandar Lashaki, M., Atkinson, J.D., Hashisho, Z., Phillips, J.H., Anderson, J.E., Nichols, M.: The role of beaded activated carbon's

pore size distribution on heel formation during cyclic adsorption/desorption of organic vapors. J. Hazard. Mater. **315**, 42–51 (2016)

Kadlec, O., Dubinin, M.M.: Comments on the limits of applicability of the mechanism of capillary condensation. J. Colloid Interface Sci. **31**(4), 479–489 (1969)

Kwiatkowski, M., Fierro, V., Celzard, A.: Confrontation of various adsorption models for assessing the porous structure of activated carbons. Adsorption **25**(8), 1673–1682 (2019)

Landers, J., Gor, G.Y., Neimark, A.V.: Density functional theory methods for characterization of porous materials. Colloids Surf. A **437**, 3–32 (2013)

Langmuir, I.: The constitution and fundamental properties of solids and liquids. Part I. Solids. J. Am. Chem. Soc. **38**(11), 2221–2295 (1916)

Langmuir, I.: The adsorption of gases on plane surfaces of glass, mica and platinum. J. Am. Chem. Soc. **40**(9), 1361–1403 (1918)

Lowell, S., Shields, J.E., Thomas, M.A., Thommes, M.: Characterization of porous solids and powders: surface area, pore size and density. Kluwer Academic Publishers, Dordrecht (2004)

Lu, S., Jin, M., Zhang, Y., Niu, Y., Gao, J., Li, C.: Chemically exfoliating biomass into a graphene-like porous active carbon with rational pore structure, good conductivity, and large surface area for high-performance supercapacitors. Adv. Energy Mater. **8**(11), 1702545 (2018)

Maddox, M.W., Quirke, N., Gubbins, K.E.: A molecular simulation study of pore networking effects. Mol. Simulat. **19**(5–6), 267–283 (1997)

Méndez-Morales, T., Ganfoud, N., Li, Z., Haefele, M., Rotenberg, B., Salanne, M.: Performance of microporous carbon electrodes for supercapacitors: comparing graphene with disordered materials. Energy Storage Mater. **17**, 88–92 (2019)

Meng, X., Wang, H.N., Song, S.Y., Zhang, H.J.: Proton-conducting crystalline porous materials. Chem. Soc. Rev. **46**(2), 464–480 (2017)

Nguyen, P.T.M., Do, D.D., Nicholson, D.: Pore connectivity and hysteresis in gas adsorption: a simple three-pore model. Colloids Surf. A **437**, 56–68 (2013a)

Nguyen, P.T.M., Fan, C., Do, D.D., Nicholson, D.: On the cavitation-like pore blocking in ink-bottle pore: evolution of hysteresis loop with neck size. J. Phys. Chem. C **117**(10), 5475–5484 (2013b)

Olivier, J.P.: Improving the models used for calculating the size distribution of micropore volume of activated carbons from adsorption data. Carbon **36**(10), 1469–1472 (1998)

Prehal, C., Koczwara, C., Jäckel, N., Schreiber, A., Burian, M., Amenitsch, H., Hartmann, M.A., Presser, V., Paris, O.: Quantification of ion confinement and desolvation in nanoporous carbon supercapacitors with modelling and in situ X-ray scattering. Nat. Energy **2**(3), 1–8 (2017)

Puziy, A.M., Poddubnaya, O.I., Gawdzik, B., Sobiesiak, M.: Comparison of heterogeneous pore models QSDFT and 2D-NLDFT and computer programs ASiQwin and SAIEUS for calculation of pore size distribution. Adsorption **22**(4–6), 459–464 (2016)

Rasmussen, C.J., Vishnyakov, A., Thommes, M., Smarsly, B.M., Kleitz, F., Neimark, A.V.: Cavitation in metastable liquid nitrogen confined to nanoscale pores. Langmuir **26**(12), 10147–10157 (2010)

Ravikovitch, P.I., Neimark, A.V.: Characterization of micro- and mesoporosity in SBA-15 materials from adsorption data by the NLDFT method. J. Phys. Chem. B **105**(29), 6817–6823 (2001)

Ravikovitch, P.I., Neimark, A.V.: Density functional theory of adsorption in spherical cavities and pore size characterization of templated nanoporous silicas with cubic and three-dimensional hexagonal structures. Langmuir **18**(5), 1550–1560 (2002a)

Ravikovitch, P.I., Neimark, A.V.: Experimental confirmation of different mechanisms of evaporation from ink-bottle type pores: equilibrium, pore blocking, and cavitation. Langmuir **18**(25), 9830–9837 (2002b)

Ravikovitch, P.I., Neimark, A.V.: Density functional theory model of adsorption on amorphous and microporous silica materials. Langmuir **22**(26), 11171–11179 (2006)

Ravikovitch, P.I., Domhnaill, S.Ó., Neimark, A.V., Schüth, F., Unger, K.K.: Capillary hysteresis in nanopores theoretical and experimental studies of nitrogen adsorption on MCM-41. Langmuir **11**(2), 4765–4772 (1995)

Ravikovitch, P.I., Vishnyakov, A., Russo, R., Neimark, A.V.: Unified approach to pore size characterization of microporous carbonaceous materials from N_2, Ar, and CO_2 adsorption isotherms. Langmuir **16**(5), 2311–2320 (2000)

Reber, M.J., Bruhwiler, D.: Bimodal mesoporous silica with bottleneck pores. Dalton T. **44**(41), 17960–17967 (2015)

Reichenbach, C., Kalies, G., Enke, D., Klank, D.: Cavitation and pore blocking in nanoporous glasses. Langmuir **27**(17), 10699–10704 (2011)

Saam, W.F., Cole, M.W.: Excitations and thermodynamics for liquid-helium films. Phys. Rev. B **11**(3), 1086–1105 (1975)

Saito, A., Foley, H.C.: Curvature and parametric sensitivity in models for adsorption in micropores. Aiche J. **37**(3), 429–436 (1991)

Saito, A., Foley, H.C.: Argon porosimetry of selected molecular sieves: experiments and examination of the adapted Horvath–Kawazoe model. Microporous Mater. **3**(4), 531–542 (1995)

Sarkisov, L., Monson, P.A.: Modeling of adsorption and desorption in pores of simple geometry using molecular dynamics. Langmuir **17**(24), 7600–7604 (2001)

Shao, J., Song, M., Wu, G., Zhou, Y., Wan, J., Ren, X., Ma, F.: 3D carbon nanocage networks with multiscale pores for high-rate supercapacitors by flower-like template and in-situ coating. Energy Storage Mater. **13**, 57–65 (2018)

Sing, K.S., Williams, R.T.: Physisorption hysteresis loops and the characterization of nanoporous materials. Adsorpt. Sci. Technol. **22**(10), 773–782 (2004a)

Sing, K.S.W., Williams, R.T.: The use of molecular probes for the characterization of nanoporous adsorbents. Part. Part. Syst. Char. **21**(2), 71–79 (2004b)

Sing, K.S.W., Rouquerol, F., Rouquerol, J., Llewellyn, P.: Adsorption by powders and porous solids (2ed). Academic Press, Oxford (2014)

Smarsly, B., Thommes, M., Ravikovitch, P.I., Neimark, A.V.: Characterization of worm-like micro- and mesoporous silicas by small-angle scattering and high-resolution adsorption porosimetry. Adsorption **11**(1), 653–655 (2005)

Sonwane, C.G., Bhatia, S.K.: Adsorption in mesopores: a molecular-continuum model with application to MCM-41. Chem. Eng. Sci. **53**(17), 3143–3156 (1998)

Steele, W.: Computer simulations of physical adsorption: a historical review. Appl. Surf. Sci. **196**(1), 3–12 (2002)

Stephen, B., Emmett, P.H., Teller, E.: Adsorption of gases in multimolecular layers. J. Am. Chem. Soc. **60**(2), 309–319 (1938)

Storck, S., Bretinger, H., Maier, W.F.: Characterization of micro- and mesoporous solids by physisorption methods and pore-size analysis. Appl. Catal. A-Gen **174**(1–2), 137–146 (1998)

Tarazona, P.: Free-energy density functional for hard spheres. Phys. Rev. A **31**(4), 2672–2679 (1985)

Tarazona, P., Marconi, U.M.B., Evans, R.: Phase equilibria of fluid interfaces and confined fluids. Mol. Phys. **60**(3), 573–595 (1987)

Thommes, M.: Physical adsorption characterization of nanoporous materials. Chem. Ing. Tech. **82**(7), 1059–1073 (2010)

Thommes, M., Smarsly, B., Groenewolt, M., Ravikovitch, P.I., Neimark, A.V.: Adsorption hysteresis of nitrogen and argon in pore networks and characterization of novel micro- and mesoporous silicas. Langmuir **22**(2), 756–764 (2006)

Vuong, T., Monson, P.A.: Monte carlo simulation studies of heats of adsorption in heterogeneous solids. Langmuir **12**(22), 5425–5432 (1996)

Walton, J.P.R.B., Quirke, N.: Capillary condensation: a molecular simulation study. Mol. Simulat. **2**(4–6), 361–391 (1989)

Wang, Y., Xia, Y.: Recent progress in supercapacitors: from materials design to system construction. Adv. Mater. **25**(37), 5336–5342 (2013)

Wang, C., Wang, X., Lu, H., Li, H., Zhao, X.S.: Cellulose-derived hierarchical porous carbon for high-performance flexible supercapacitors. Carbon **140**, 139–147 (2018)

Wongkoblap, A., Intomya, W., Somrup, W., Charoensuk, S., Junpirom, S., Tangsathitkulchai, C.: Pore size distribution of carbon with different probe molecules. Eng. J. **14**(3), 45–56 (2010)

Xia, K., Gao, Q., Jiang, J., Hu, J.: Hierarchical porous carbons with controlled micropores and mesopores for supercapacitor electrode materials. Carbon **46**(13), 1718–1726 (2008)

Young, C., Lin, J., Wang, J., Ding, B., Zhang, X., Alshehri, S.M., Ahamad, T., Salunkhe, R.R., Hossain, S.A., Khan, J.H., Ide, Y., Kim, J., Henzie, J., Wu, K.C., Kobayashi, N., Yamauchi, Y.: Significant effect of pore sizes on energy storage in nanoporous carbon supercapacitors. Chem. Eur. J. **24**(23), 6127–6132 (2018)

Zhu, G., Chen, T., Wang, L., Ma, L., Hu, Y., Chen, R., Wang, Y., Wang, C., Yan, W., Tie, Z., Liu, J., Jin, Z.: High energy density hybrid lithium-ion capacitor enabled by Co_3ZnC@N-doped carbon nano-polyhedra anode and microporous carbon cathode. Energy Storage Mater. **14**, 246–252 (2018)